Article

Selective Deposition of Candle Soot on a Cellulose Membrane for Efficient Solar Evaporation

Mamoon Ur Rashid, Zeeshan Tahir, Sungdo Kim, Joon I. Jang,* and Yong Soo Kim*

Cite This: *ACS Omega* 2021, 6, 31366−31374

Read Online

ACCESS | Metrics & More | Article Recommendations | Supporting Information

ABSTRACT: Owing to their natural abundance, seawater together with sunlight has a potential to meet the global challenges in terms of water scarcity and energy crisis. Herein, we demonstrate a solar vapor generator composed of an inner flame candle soot (IFCS) deposited on a cellulose filter paper (FP) prepared by a simple two-step process. The resultant IFCS/FP device exhibits a high photothermal conversion ability owing to the broadband solar absorption of the IFCS layer along with the multiple scattering of the incoming sunlight in the porous microstructure of the cellulose FP. Additionally, the low thermal conductivity of the IFCS effectively localizes the photothermally generated heat at the IFCS/ FP surface, thereby significantly suppressing the conduction heat losses to the underlying bulk water. Meanwhile, the capillary action of the FP supplies an adequate amount of water to the heated

surface for accelerating the evaporation process. Benefitting from the synergistic effect of these characteristics, the IFCS/FP achieves high evaporation rates of ∼1.16 and ∼4.09 kg m^{-2} h^{-1} and their corresponding efficiencies of ∼75.1 and 90.9% under one and three sun illumination, respectively. Moreover, the IFCS/FP device presents an excellent longevity owing to the persistent performance over 15 repeated cycles under one and three sun illumination. Hence, the facile fabrication, fine mechanical strength, desalination, and the salt-resistance ability of our IFCS/FP make it a suitable candidate for practical applications.
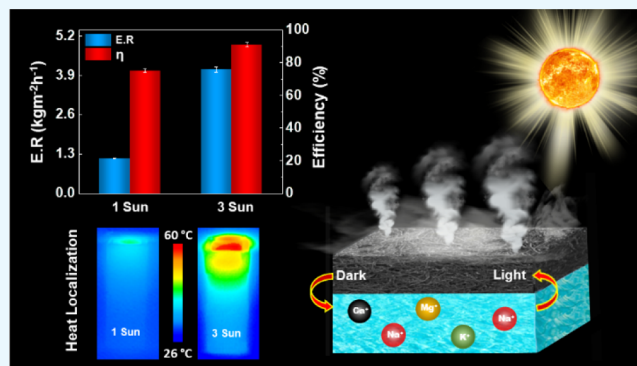
■ INTRODUCTION

Due to the rapid increase in the world's population and the continual pollution of available freshwater resources, water scarcity is increasing at an alarming rate.[1−3] As per a report, nearly 3.6 billion of the world population lack an access to clean water, which is estimated to be nearly 6 billion by 2050.[4] Therefore, developing inexpensive and efficient methods for wastewater treatment is highly desirable.[5,6] Numerous techniques such as vapor compression,[7] multiple-effect distillation,[8] and reverse osmosis[9,10] have been established to alleviate the freshwater shortage. However, these techniques demand either a high electrical consumption or complex supporting/installation structures, thereby hindering their applicability, particularly for the off-grid communities and the developing regions.[7,11,12] Solar distillation has emerged as a potential alternative owing to the fact that it utilizes the eco-friendly, cost-free, and sustainable source of energy for eliminating the impurities from the contaminated or sea water.[13−15] Accordingly, the relevant technology has rapidly transited from the traditional ways of vaporizing the bulk water via optical concentrators or volumetric solar absorbers toward the realization of low-cost and efficient interfacial solar vapor generators.[16−21] In principle, an interfacial solar vapor generator transforms the solar energy to heat and confines it at the evaporation surface wherein a suitable amount of water

supply maximizes the vaporization rate.[22,23] Therefore, the performance of such devices mainly depends on four key factors: (i) photothermal conversion, (ii) heat localization at the evaporation surface, (iii) effective capillary action for the controlled water transport, and (iv) water evaporation.[24−26] In this regard, a variety of innovative photothermal materials such as plasmonic nanoparticles, organic polymers, and semi-conducting, functional, and biomass materials have been employed as per their individual appealing character-istics.[5,27−33] However, carbon is the most widely studied material for solar vapor generation owing to its natural abundance and excellent light to heat conversion capability. Consequently, it has been widely investigated in both natural and synthetic forms such as beads, nanotubes, exfoliated graphite, porous graphene, and vitreous foams for solar vapor generation.[24,34−37]
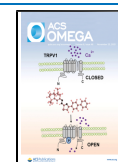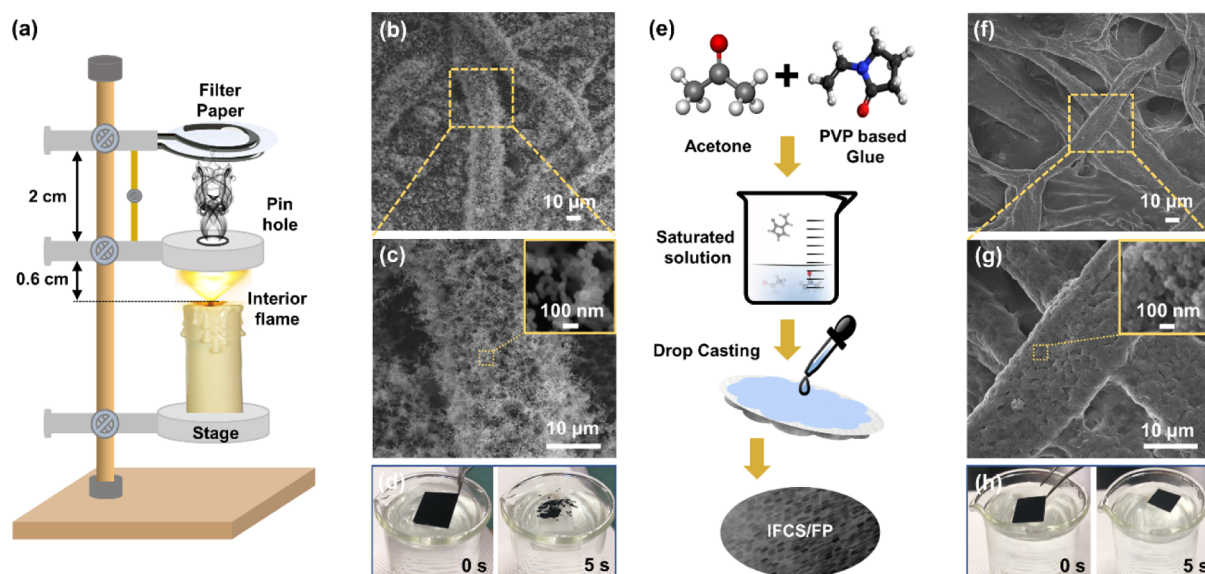
Figure 1. Two-step fabrication process of the IFCS/FP. (a) Schematic of the homebuilt setup for the controlled collection of IFCS on the FP. (b,c) FE-SEM images show weak adhesion between the as-deposited IFCS and the FP. The inset reveals a lack of cohesion among the IFCS particles as well. (d) Time-lapse digital images showing the segregation of the as-deposited IFCS and the FP owing to their weak bonding. (e) Stepwise preparation of the PVP-based saturated glue solution. (f,g) FE-SEM images of the IFCS/FP confirm strong bonding, not only between the IFCS and the FP but also among the IFCS particles (inset) as well. (h) Time-lapse digital images present the excellent floatability of the IFCS/FP owing to strong adhesion between its constituents, that is, IFCS and FP.

Soot is a complex mixture of carbon-based compounds resulting from the incomplete combustion of hydrocarbons.[38] It has been extensively studied as an electrode in an energy storage device owing to its superior physicochemical and electrochemical supercapacitance.[39] Note that the physical and chemical properties of the extracted soot profoundly depend on the source's (hydrocarbon) composition.[40] For instance, the flame soot derived from paraffin wax candles exhibits beneficial characteristics for solar vapor generation such as high solar absorption, low thermal conductivity, tunable hydrophobicity, stability, and the relatively low toxicity.[39−42] However, these features greatly vary between the soot collected from the flame tip and the inner region based on their distinct degree of oxidation (combustion).[40] Therefore, regardless of several attempts on solar vapor generation via the candle flame soot, the detailed analysis regarding the soot origin (flame region) is still missing. In addition, majority of the soot-based solar vapor generators follow sophisticated synthesis procedures, as mentioned in Table S1.

In this work, we report a low-cost solar vapor generator composed of inner flame candle soot (IFCS) coated on a cellulose membrane, that is, a filter paper (FP). The IFCS/FP device is fabricated via a simple two-step procedure; (i) selective deposition of the hydrophobic soot from the inner flame region of the candle on a super hydrophilic FP and (ii) maximization of the adhesion between the as-deposited IFCS and the FP by gluing. Interestingly, the combination (IFCS and FP) yields a hydrophobic/hydrophilic interface that naturally renders the IFCS/FP with the capability of floating. Besides, the IFCS/FP also possesses a high photothermal conversion capability owing to the cumulative effect of broadband solar absorption of the IFCS layer and the potential trapping of the incoming sunlight in the porous morphology of the FP. In addition, the low thermal conductivity of the IFCS layer effectively localizes the photothermally generated heat at the evaporation surface wherein the capillary action of the FP

supplies suitable proportion of water to the heated surface to facilitate the evaporation process. The combined effect of the above-mentioned characteristics endows our IFCS/FP with high evaporation rates ~1.16 and ~4.09 kg m^{-2} h^{-1} and efficiencies ~75.1 and ~90.9% under 1 and 3 sun illumination, respectively. Moreover, the stability and durability of the IFCS/FP were demonstrated by the persisting performance over several runs, while the mechanical strength was tested through a systematic exposure to 0.3 kg weight in one- and twofold states. Finally, the desalination capability was tested via an inductively coupled plasma (ICP) method, indicating a decrease in the ion concentration after desalination, while a complete recyclability of the device was ensured through a self-cleaning (salt resistance) capability.

RESULTS AND DISCUSSION

Figure 1 illustrates the systematic fabrication process of the IFCS/FP device. Initially, the IFCS is deposited on a FP in a controlled manner via a homebuilt setup, as shown schematically in Figure 1a. The setup consists of three adjustable holders for candle, pinhole, FP, and a lock bar to ensure a constant distance of ~2 cm between the pinhole and the FP. Additionally, the distance between the candle wick top and the pinhole was kept at ~0.6 cm during the entire soot collection process. The pinhole aperture (diameter, ~0.3 cm) is located at the exact center of the candle flame to completely block the flame tip soot and allow only the inner flame soot to accumulate on the FP. The low-resolution field-emission scanning electron microscopy (FE-SEM) image shown in Figure 1b confirms the successful deposition of the IFCS on the porous microstructure of the FP. However, the high-resolution FE-SEM image (Figure 1c) acquired from the highlighted region of Figure 1b reveals weak bonding not only between IFCS and FP but also among the individual IFCS particles (inset) as well, which is further verified by the time-lapse digital images (Figure 1d) showing a swift segregation of
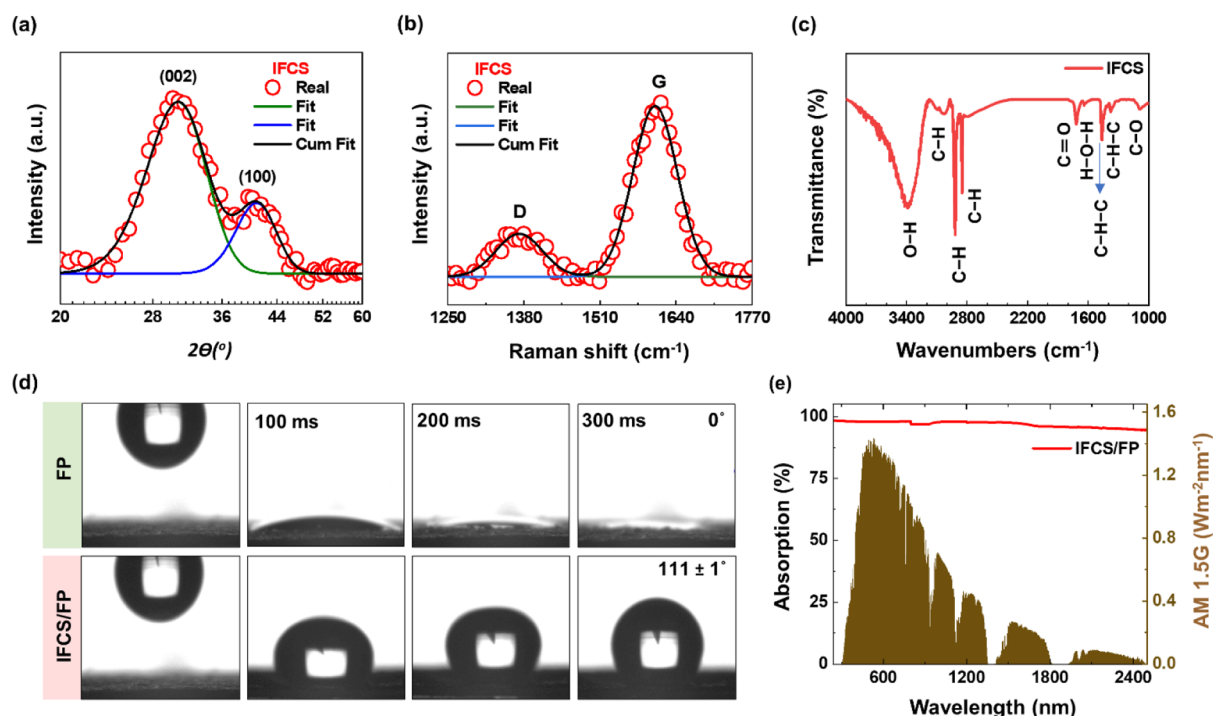
Figure 2. Characterization of the IFCS. (a) XRD pattern of IFCS powder. The XRD peaks at 30 and 41° correspond to the (002) and (100) planes of the hexagonal lattice of graphite, respectively. (b) Raman spectrum of IFCS powder. The peaks at 1370 and 1600 cm^{-1} represent the D and G bands of carbon, whereby the high intensity of the G band also suggests the graphitization of the IFCS. (c) FTIR spectrum of the IFCS deposited on a ZnSe substrate. (d) Time-lapse contact-angle measurement of the FP shows a nearly 0° angle, indicating its hydrophilic nature, while the IFCS/FP presents a large contact angle of ~111 ± 1° owing to the deposition of the hydrophobic IFCS. (e) Absorption spectra of the IFCS/FP (red) in the range of 250−2500 nm. The high absorption across the entire solar spectrum signifies the excellent photothermal conversion capability of the IFCS/FP.

IFCS and FP upon a 5 s exposure to water. In order to strengthen the bonding between IFCS and FP, a saturated solution of polyvinylpyrrolidone (PVP)-based glue and acetone (1:4) was prepared at room temperature via magnetic stirring and drop casted on the rear side of the soot-deposited FP, as shown schematically in Figure 1e. The IFCS/FP device was dried in the ambient environment for 15 min. Figure 1f shows the low-resolution FE-SEM image of the IFCS/FP after gluing. The relatively smooth surface texture readily displays the gluing effect, yielding strong adhesion between IFCS and FP, which is very evident from the high-resolution FE-SEM image (Figure 1g) captured from the highlighted portion of Figure 1f. The inset now reveals a stronger cohesion among the individual IFCS particles as well. Furthermore, the time-lapse digital images of Figure 1h also signify a stronger bonding between IFCS and FP owing to their adhesion upon a 5 s exposure to water. The long-term stable floatability of the IFCS/FP was tested over a longer period of 30 days and an exposure to the harsh ultrasonic environment, as shown in Figure S1 and Video S1, respectively.

The crystal structure of IFCS powder was analyzed by X-ray diffraction (XRD) and micro-Raman spectroscopy, respectively. Figure 2a presents the XRD spectrum of the IFCS. The broader peaks with their characteristic low intensities indicate the low crystalline quality of the IFCS particles. The diffraction peaks at ~30 and ~41° correspond to the (002) and (100) planes of the hexagonal graphite lattice, thereby suggesting the graphitization of the IFCS (JSPDs #41-1487).[39] Figure 2b shows the Raman spectrum of the IFCS. The Raman peak at 1370 cm^{-1} corresponds to the D-band of carbon, which basically signifies the distortion of the sp^2-hybridized crystalline

structure, while the peak at 1600 cm^{-1} is associated with the G-band, indicating the stretching of the C−C bonds in the graphite materials. Additionally, the high intensity of the G-band demonstrates that the IFCS is rich in sp^2-hybridized graphite, which is not only consistent with the XRD analysis in terms of graphitization of IFCS but also indicates its hydrophobic nature.[43,44]

The chemical composition of the IFCS was characterized by Fourier-transform infrared (FTIR) spectroscopy, which reveals that the candle soot is a mixture of branched hydrocarbons such as carboxylic groups, methyl, and methylene groups. Figure 2c presents the FTIR spectrum of the IFCS collected on a ZnSe substrate. The peaks at 3429 and 1639 cm^{-1} represent the stretching vibrations of the surface hydroxyl group (−OH) and the H_2O-bending mode, respectively. Generally, the C−H stretching bands occur in the range from 3300 to 2800 cm^{-1}. Therefore, the band at 2954 cm^{-1} arises from the asymmetric stretching vibration of CH_2, while the two peaks at 2918 and 2849 cm^{-1} are attributed to the symmetric and asymmetric vibrations of the CH_3 moiety, respectively. Moreover, dips around 1718 and 1089 cm^{-1} indicate the presence of carbonyl (C=O) and carboxy (C−O) groups, respectively. The peak at 1462 cm^{-1} manifests the H−C−H symmetric bending mode of CH_3, while the band at 1377 cm^{-1} corresponds to the CH stretching vibration of the CH_2 functional group.[40,45] In addition, the comparison of the characteristic CH_3 bands (2918 and 2849 cm^{-1}) of the candle soot collected from the inner flame region and the flame tip is shown in Figure S2a. Clearly, the soot from the inner flame region shows strong and intense CH_3 bands, signifying the presence of a large proportion of CH_3 (organic), resulting from the incomplete
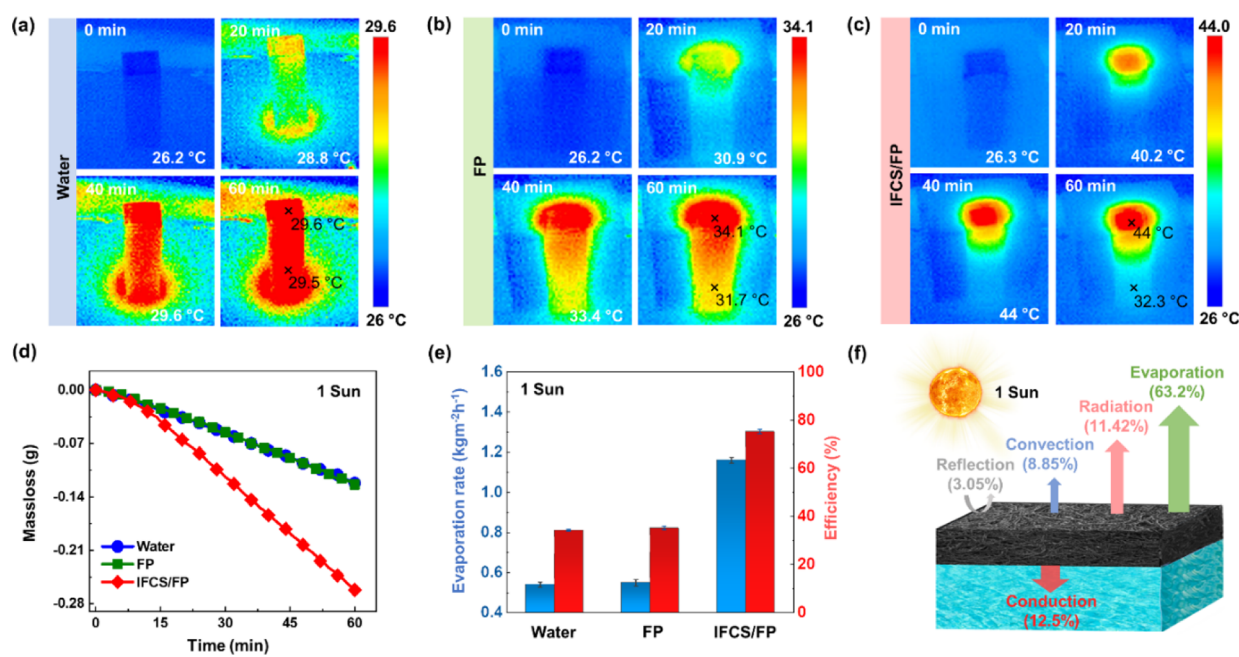
Figure 3. Thermal profile, performance, and heat management under one sun illumination. (a–c) Time-lapse thermal images of water, the FP, and the IFCS/FP. Clearly, the IFCS/FP shows a superior heat localization as evident from the large temperature difference between the surface and bulk water. Besides, the high surface temperature of the IFCS/FP shows its excellent photothermal conversion capability. (d) Mass loss as a function of time for pure water (blue), the FP (green), and the IFCS/FP (red). (e) Estimated evaporation rate and efficiency of pure water, the FP, and the IFCS/FP. (f) Schematic representation of the inevitable heat losses via the IFCS/FP under one sun illumination.

combustion/oxidation of the candle wax.[40] The stronger CH_3 bands also demonstrate the hydrophobic nature of the IFCS, which is consistent with Raman analysis mentioned in Figure 2b. In order to directly confirm the hydrophobic nature of the IFCS, the water contact angles were measured. Figure 2d shows the time-lapse contact angle images with an adjacent time interval of 100 ms. The nearly ∼0° contact angle at 300 ms manifests the superhydrophilic nature of the FP, indicating the presence of the strong capillary action, thereby making the FP unable to float on the water surface, as shown in Figure S2c. However, upon the deposition of the IFCS layer, a higher contact angle ∼111 ± 1° is observed at 300 ms, signifying the hydrophobic nature of the IFCS. Consequently, the IFCS/FP device not only floats steadily on the water surface (Figure S2d) but also exhibits the capillary action essential for the effective transport of water to the evaporation surface.

Photothermal conversion is the ability of a device to convert sunlight into heat and is considered as one of the essential prerequisites of an efficient solar vapor generator. Figure 2e shows the absorption spectrum of the IFCS/FP over the energy distribution of a solar simulator (AM 1.5G). The IFCS/FP shows a high absorption (>95%) across the entire solar spectrum, indicating the superior photothermal conversion capability, which is attributed to the combined effect of broadband solar absorption of the IFCS (evident from its black appearance) and multiple scattering of the incident sunlight in the porous morphology of the FP. The absorption spectrum is estimated using the equation $A = 1 - (R + T)$, where R and T represent diffuse reflectance and transmittance, respectively, as shown in Figure S3a,b.

Heat localization plays a significant role in the suppression of heat losses to the underlying bulk water, yielding enhanced solar vapor generation.[24,25] The heat localization capability of the IFCS/FP was evaluated by monitoring the dynamic temperature change of the surface and the bulk water over a period of 1 h. For this purpose, a thermal camera was used, whereby the images were taken every 20 min to probe the real-time temperature variations. Figure 3a–c shows the time-lapse thermal images of pure water, the FP, and the IFCS/FP, respectively, under one sun illumination. The thermal profile of pure water (Figure 3a) at 60 min indicates a nearly uniform temperature distribution across the entire beaker due to the high thermal conductivity of water ∼0.61 $Wm^{-1} K^{-1}$.[46] The negligible temperature difference ∼0.1 °C between the surface and bulk water reveals the absence of heat localization. In contrast, both the FP and the IFCS/FP exhibit considerable heat localization as evident from the nonuniform temperature distribution across the container, as shown in Figure 3b,c, respectively. Furthermore, the IFCS/FP clearly demonstrates a superior heat localization owing to the relatively low thermal conductivity of the IFCS layer (0.07 $Wm^{-1} K^{-1}$)[28] relative to that of the bare FP (0.10 $Wm^{-1} K^{-1}$).[47] Accordingly, the thermal image at 60 min for the IFCS/FP manifests a higher temperature difference ∼11.7 °C between the surface and the bulk water compared to that of the FP (∼2.4 °C), confirming the excellent heat localization capability of our IFCS/FP device. In addition, the time-lapse thermal images of the IFCS/FP (Figure 3c) illustrate a rapid increase of the surface temperature to a peak value of ∼44 °C, which is higher than that of both the FP (34.1 °C) and pure water (29.6 °C), thereby verifying the excellent photothermal conversion capability of the IFCS/FP and is consistent with the absorption measurements of Figure 1e. Note that the FP was floated artificially for these measurements, as explained in Figure S4. The detailed time-lapse thermal images for pure water, the FP, and the IFCS/FP under one sun illumination are shown in Figure S5.

Based on the above analysis, the IFCS/FP exhibits all the parameters important for efficient solar vapor generation. The performance of the IFCS/FP device was evaluated by
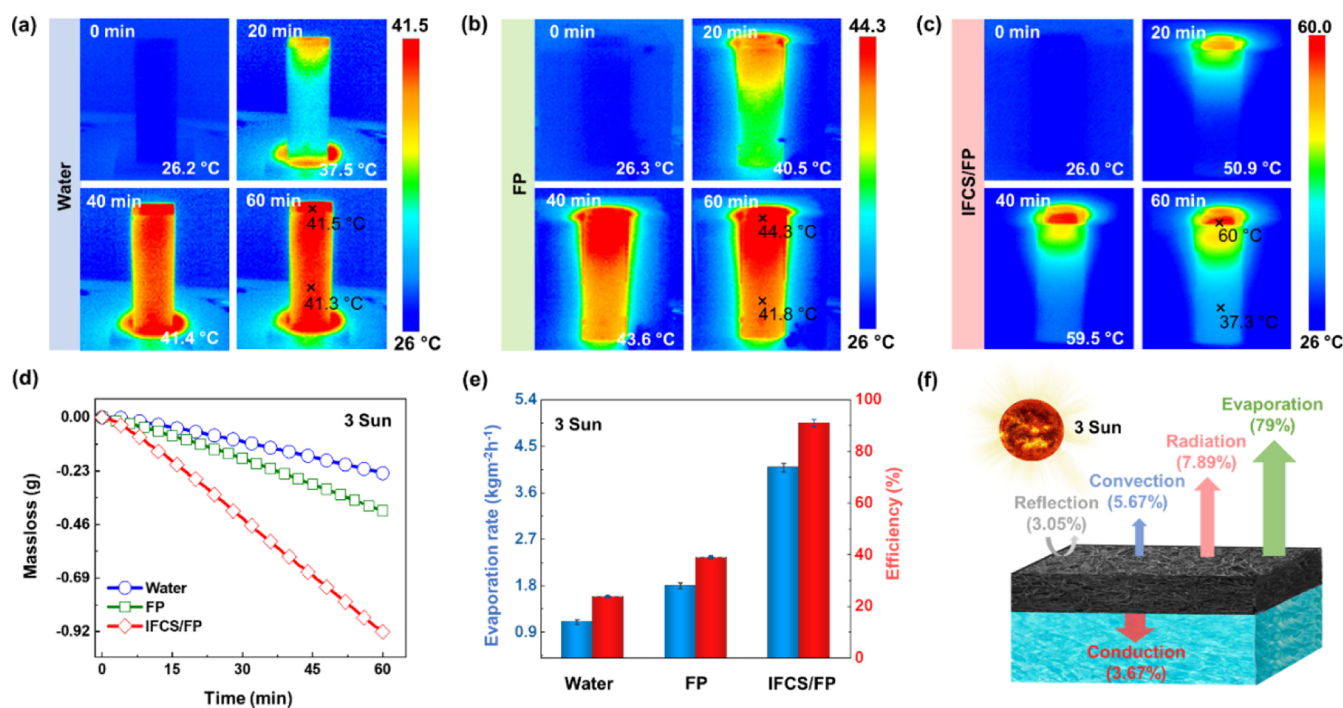
Figure 4. Thermal profile, performance, and heat losses under three sun illumination. (a−c) Time-lapse thermal images of water, the FP, and the IFCS/FP. Clearly, the IFCS/FP shows the superior heat localization as evident from the large temperature difference between the surface and bulk water. (d) Mass loss as a function of time for pure water (blue), the FP (green), and the IFCS/FP (red). (e) Estimated evaporation rate and efficiency of pure water, the FP, and the IFCS/FP. (f) Schematic representation of the inevitable heat losses via the IFCS/FP under three sun illumination.

monitoring the mass loss of bulk water over a period of 1 h using a homebuilt setup shown in Figure S6. The photo-thermal conversion efficiency was calculated using the equation[48,49]

$$\eta \ [\%] = \frac{\dot{m} h_{lv}}{C_{opt} P_o} \times 100 \tag{1}$$

where $\dot{m}$ (kg m^{-2} s^{-1}) is the mass change due to evaporation under the steady-state condition, $P_o = 1$ kW m^{-2} is the power density of the incoming solar energy, C_{opt} is the optical concentration at the device surface, and h_{lv} represents the total heat enthalpy of liquid−vapor phase transition, which is equal to the sum of the latent heat and the sensible heat enthalpy as given by

$$h_{lv} = \lambda_{lv} + C_p(T_2 - T_1) \tag{2}$$

where $\lambda_{lv} = 2257$ kJ kg^{-1} is the latent heat of water vaporization at standard atmospheric pressure, $C_p = 4.2$ kJ kg^{-1} K^{-1} is the specific heat capacity, and $T_2 - T_1$ represents the difference in the temperature of water.

Figure 3d shows the mass loss for pure water, the FP, and the IFCS/FP under one sun illumination. The IFCS/FP shows a highest mass loss of ∼0.262 g compared to that of the FP (0.124 g) and pure water (0.122 g). The corresponding evaporation rates and photothermal conversion efficiencies are plotted in Figure 3e. The evaporation rates for pure water, the FP, and the IFCS/FP were found to be 0.54, 0.55, and 1.16 kg m^{-2} h^{-1}, while their associated photothermal conversion efficiencies were calculated as 34.1, 35, and 75.1%, respectively. It was observed that the efficiency of the FP is approximately the same as that of pure water, despite the heat localization. This is due to the weak photothermal conversion capability of

the FP as evident from its low solar absorption spectrum, as shown in Figure S3b. In order to account for the natural evaporation that occurs in the absence of sunlight, the dark evaporation rates were measured for pure water, the FP, and the IFCS/FP (Figure S7). The net efficiency of the IFCS/FP after substracting the dark performance was found to be ∼63.2%, which is still 3 and 2.8 times higher than that of pure water and the bare FP, respectively. This enhanced performance is attributed to the cumulative effect of high photothermal conversion, effective capillary action, and the heat localization of the IFCS/FP device. The inevitable heat losses that occur during the solar vapor generation process using the IFCS/FP are schematically shown in Figure 3f. Under one sun illumination, the heat losses from the IFCS/FP surface to the surrounding such as reflection, convection, and radiation were found to be ∼3.05, ∼8.85, and ∼11.42%, respectively, while the conduction heat loss to the underlying bulk was calculated as 12.5%. The details related to the calculation of heat losses are mentioned in Note S1.

The performance of the IFCS/FP was also tested under intense solar irradiation. Figure 4a−c shows the time-lapse thermal images of pure water, the FP, and the IFCS/FP, respectively, under three sun illumination. These thermal profiles present nearly the same trend as those under one sun illumination. However, an enhanced heat localization was observed for the IFCS/FP as evident from the high temperature difference ∼22.7 °C between the surface and the bulk water relative to pure water (0.2 °C) and the FP (2.5 °C). Consequently, the conduction heat losses to the underlying bulk water were effectively suppressed, yielding a significant increase in the performance of the IFCS/FP under three sun illumination. Figure S8 shows the detailed time-lapse thermal images for pure water, the FP, and the IFCS/FP under

3 kW m^{-2}. Figure 4d shows the mass loss of pure water, the FP, and the IFCS/FP under three sun irradiation. The IFCS/FP presents a higher mass loss of ~0.921 g compared to the FP (0.401 g) and pure water (0.240 g). The estimated evaporation rates and photothermal conversion efficiencies of pure water, the FP, and the IFCS/FP are shown in Figure 4e. The evaporation rates for pure water, the FP, and the IFCS/FP were found to be 1.1, 1.8, and 4.09 kg m^{-2} h^{-1}, while their corresponding photothermal conversion efficiencies were calculated as 23.6, 38.8, and 90.9%, respectively. Considering natural evaporation (Figure S7) into account, the net efficiency of the IFCS/FP is 79% which is still 3.35 and 2.04 times higher than that of the pure water and the FP, respectively. Nevertheless, the efficiency of the IFCS/FP under three sun illumination is ~1.25 times higher than that under one sun illumination, which is attributed to the significant reduction in the heat losses, particularly the conduction heat loss owing to the enhanced heat localization of the IFCS/FP. Figure 4f schematically shows the heat losses under three sun illumination. The reflection, convection, and radiation heat losses were computed as 3.05, 5.67, and 7.89%, respectively, while the conduction heat loss is estimated as 3.67% (details are given in Note S1 and Table S2).

Figure 5a shows the evaporation rate of the IFCS/FP over 15 repeated cycles using distilled water. The nearly persistent
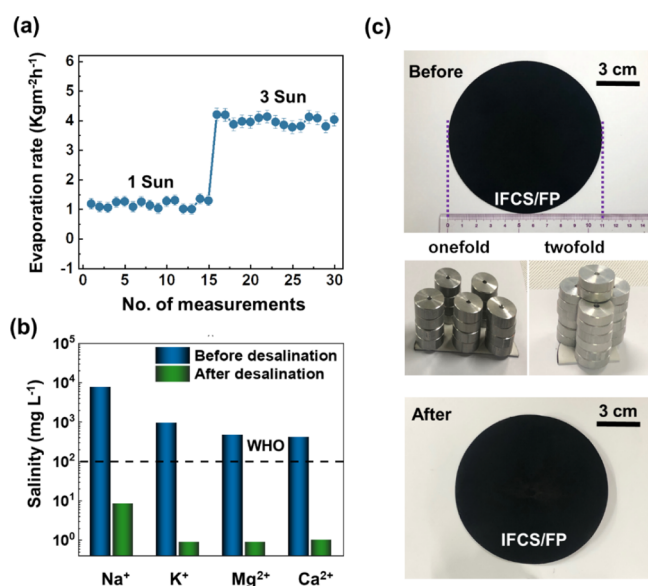

Figure 5. Stability, desalination, and mechanical flexibility of the IFCS/FP device. (a) Evaporation rate of the IFCS/FP using the distilled water over 15 repeated runs under one and three sun illumination. The nearly persistent performance indicates the excellent stability of our IFCS/FP. (b) Salinity of artificial sea water before and after desalination using the IFCS/FP. A clear decrease in the ion concentration demonstrates the desalination capability of the IFCS/FP. (c) Digital images of IFCS/FP before and after under 0.3 kg weight in one and twofold states, which shows no clear sign of damage, thereby confirming its mechanical strength and flexibility.

performance under one and three sun illumination indicates the excellent stability of our IFCS/FP. The desalination performance of the IFCS/FP was examined by measuring the ion concentration of artificial seawater before and after desalination. The homebuilt desalination setup is shown in Figure S9. Figure 5b shows a significant decrease in the ion

concentration after desalination, making it suitable for drinking as per the standards of World Health Organization (WHO). The mechanical strength and flexibility of a large-scale (diameter: 11 cm) IFCS/FP device were tested under 0.3 kg weight in one and twofold states, as shown in Figure 5c. The digital images acquired before and after the removal of weights show no clear evidence of damage, indicating the good mechanical strength and flexibility of IFCS/FP.

Figure 6a schematically explains the salt-resistance (self-cleaning/recyclability) of the IFCS/FP device. During the desalination process under sunlight, salt crystals (white) start to accumulate in the micropores and on the surface of the IFCS/FP, yielding a higher concentration of salt in the water contained within the device as compared to the bulk water underneath. This concentration imbalance stimulates continuous diffusion of water from the underlying bulk water toward the device, which eventually leads to a complete removal of the salt from the device. However, it is hard to achieve such a condition in the presence of sunlight due to the rapid water evaporation, causing the accumulation of salt at a higher rate than its diffusion back to the bulk water. On the contrary, the slow evaporation process in the absence of sunlight (dark) allows salt diffusion back to the bulk water, thereby self-recycling the IFCS/FP device.[50] In order to confirm the self-cleaning capability, the performance of the IFCS/FP device was monitored under one sun illumination for a period of 8 h, as shown in Figure 6b. As expected, the performance of the device decreases gradually with the passage of time due to the accumulation of salt crystals in the micropores of the IFCS/FP device, therefore hindering the net flow of water to the evaporation surface. Figure 6c presents the SEM image of the IFCS/FP after desalination for 8 h. The image clearly shows the accumulation of salt clusters (dashed green circles) in the micropores of the IFCS/FP. Additionally, the digital image in the inset reveals the formation of salt aggregates (white) on the IFCS/FP surface. However, a complete recyclability of the IFCS/FP device was observed by keeping it in the dark for 4 h, whereby the accumulated salt diffuses back to the underlying bulk water as evident from the SEM image (Figure 6d) acquired from the same region of the IFCS/FP as Figure 6c. The dark evaporation rate of the IFCS/FP during the recovery period of 4 h is plotted in Figure S10. Afterward, the device performance was tested again for 8 h under one sun illumination. As shown in Figure 6e, the recycled device follows nearly the same pattern as Figure 6b, indicating the excellent self-recyclability of our IFCS/FP device.

■ SUMMARY

In summary, we have demonstrated efficient solar vapor generation via our IFCS/FP device, composed of IFCS collected on a cellulose FP. The IFCS/FP device is fabricated via a simple two-step process. Owing to the hydrophobic and superhydrophilic nature of the IFCS and the FP, respectively, the final device is capable of floating which is considered imperative for a self-floating solar vapor generator. Systematic analyses of the IFCS/FP reveal that our device exhibits all the important parameters necessary for an efficient solar vapor generator. For instance, the high photoabsorption and the porous morphology of the IFCS/FP provide the essential light-to-heat conversion capability, while the low thermal conductivity offers the significant heat localization, substantial for reducing the heat losses to the underlying bulk water. In addition, the capillary action of the IFCS/FP supplies a
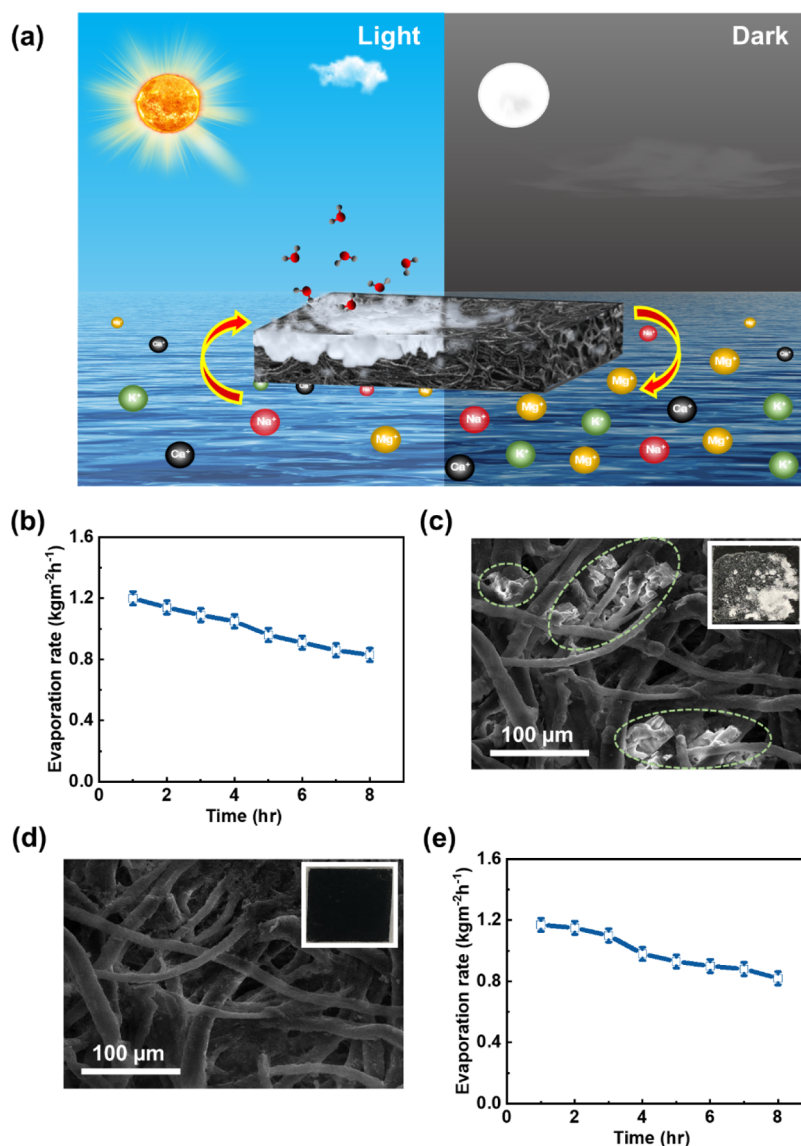
Figure 6. Salt-resistance or self-recyclability of the IFCS/FP device. (a) Schematic illustration of the salt-resistance ability of the IFCS/FP. During desalination, the salt clusters accumulate on the surface and inside the microstructure of the IFCS/FP (left panel) while they diffuse back to the bulk water in the dark (right panel). (b) Evaporation rate of the IFCS/FP using seawater over a period of 8 h (c) SEM image showing the presence of salt clusters (dashed green circles) in the micropores of the IFCS/FP after desalination for 8 h. The digital image in the inset reveals the presence of salt aggregates on the IFCS/FP surface as well. (d) SEM image acquired from the same region of the IFCS/FP as Figure 6c, however, after keeping it in the dark for 4 h. The images reveal a successful removal of salt clusters from the micropores and surface (inset) of the IFCS/FP. (e) Evaporation rate of the recycled IFCS/FP over a period of 8 h. The nearly same trend of the evaporation rates before and after the recycling confirms the excellent self-cleaning capability of our IFCS/FP device.

suitable amount of water to the evaporator surface for enhancing the evaporation process. Consequently, the IFCS/FP device attained high efficiencies of ~75.1 and 90.9% under one and three sun illumination. Besides, the facile fabrication, excellent stability, mechanical strength, and the salt-resistance capability of the IFCS/FP suggest that our device could potentially be applied for a large-scale solar desalination and waste water treatment.

■ EXPERIMENTAL SECTION

Materials. Advantec FPs (no. 2, 110 mm diameter) were purchased from Hyundai Micro. The candles were purchased from Myung Kwang chemical industries. AMOS glue stick was mixed with acetone in a 1:4 ratio to prepare saturated glue solution.

Characterizations. FE-SEM images were taken by a JEOL JSM-6500F microscope. The XRD 2θ scan was executed via a lab source (4-circle) X-ray diffractometer (wavelength = 1.5406 Å; Cu K$_\alpha$1, D8 Discover, Bruker). The Raman spectrum at room temperature was recorded using a 473 nm excitation source. FTIR spectroscopy in the range 4000−1000 cm^{-1} was acquired using a Bruker Invenio R spectrometer. The water contact angles of the samples were measured by SEO, Phoenix 300. The diffuse reflectance and transmittance spectra were acquired using a Varian, Cary5000 spectrometer, equipped with an integrating sphere. An Abet Tech Inc. 10,500 solar simulator was used to replicate the natural sunlight. The temperature profiles were measured using a Testo-868 (160 × 120 pixels) thermal imager. A 1.5 × 1.5 cm^2 IFCS/FP was placed in a square container under the solar

simulator at one and three sun position on an electronic balance (Vibra, AJH-220E-D) to record the mass change of bulk water. The ion concentrations of saline and desalinated water were analyzed by ICP mass spectrometry.

■ ASSOCIATED CONTENT

ⓢ Supporting Information

The Supporting Information is available free of charge at https://pubs.acs.org/doi/10.1021/acsomega.1c05348.

Long-term stable floatability of the IFCS/FP device; comparison of the IFCS and the flame tip soot; diffuse reflectance, transmittance, and absorption of FP (green) and IFCS/FP (red); artificial floating of the FP; time-lapse thermal images with an adjacent time interval of 5 min under 1 sun irradiation; schematic of the homebuilt setup used for monitoring the mass loss and thermal profile of the IFCS/FP device; evaporation rates and efficiencies in the dark environment; time-lapse thermal images with an adjacent time interval of 5 min under three sun illumination; homebuilt setup for desalination; dark evaporation rates monitored during the recycling period of 4 h; inevitable heat loss measurements; comparison with the reported soot-based solar vapor generators; and details of calculated evaporation rates, photothermal conversion efficiencies, and heat losses under one and three sun illumination for the IFCS/FP device (PDF)

Ultrasonication (MP4)

■ AUTHOR INFORMATION

Corresponding Authors

Joon I. Jang − *Department of Physics, Sogang University, Seoul 04107, South Korea;* ⓞ orcid.org/0000-0002-1608-8321; Email: jjcoupling@sogang.ac.kr

Yong Soo Kim − *Department of Physics and Energy Harvest-Storage Research Center, University of Ulsan, Ulsan 44610, South Korea;* ⓞ orcid.org/0000-0001-8641-1035; Email: yskim2@ulsan.ac.kr

Authors

Mamoon Ur Rashid − *Department of Physics and Energy Harvest-Storage Research Center, University of Ulsan, Ulsan 44610, South Korea;* ⓞ orcid.org/0000-0002-9476-5009

Zeeshan Tahir − *Department of Physics and Energy Harvest-Storage Research Center, University of Ulsan, Ulsan 44610, South Korea;* ⓞ orcid.org/0000-0002-9402-5297

Sungdo Kim − *Department of Physics and Energy Harvest-Storage Research Center, University of Ulsan, Ulsan 44610, South Korea;* ⓞ orcid.org/0000-0002-5472-9134

Complete contact information is available at:
https://pubs.acs.org/10.1021/acsomega.1c05348

Author Contributions

M.U.R. and Z.T. contributed equally to this work. M.U.R. and Z.T. fabricated the samples and performed characterizations. S.K. measured the performance of solar steam generation. Y.S.K. and J.I.J. supervised the experiments and analyzed the data. M.U.R. led the manuscript preparation. All the authors contributed to the manuscript writing and reviewed the manuscript and have given approval to the final version of the manuscript.

Notes

The authors declare no competing financial interest.

■ REFERENCES

(1) Jones, E.; Qadir, M.; van Vliet, M. T. H.; Smakhtin, V.; Kang, S.-m. The State of Desalination and Brine Production: A Global Outlook. *Sci. Total Environ.* **2019**, *657*, 1343−1356.

(2) Oki, T.; Kanae, S. Global Hydrological Cycles and World Water Resources. *Science* **2006**, *313*, 1068−1072.

(3) Rijsberman, F. R. Water Scarcity: Fact or Fiction? *Agric. Water Manage.* **2006**, *80*, 5−22.

(4) Boretti, A.; Rosa, L. Reassessing the Projections of the World Water Development Report. *npj Clean Water* **2019**, *2*, 15.

(5) Gong, F.; Wang, W.; Li, H.; Xia, D.; Dai, Q.; Wu, X.; Wang, M.; Li, J.; Papavassiliou, D. V.; Xiao, R. Solid Waste and Graphite Derived Solar Steam Generator for Highly-Efficient and Cost-Effective Water Purification. *Appl. Energy* **2020**, *261*, 114410.

(6) Li, Z.; Wang, C.; Su, J.; Ling, S.; Wang, W.; An, M. Fast-Growing Field of Interfacial Solar Steam Generation: Evolutional Materials, Engineered Architectures, and Synergistic Applications. *Sol. RRL* **2019**, *3*, 1800206.

(7) Panagopoulos, A. Techno-Economic Evaluation of a Solar Multi-Effect Distillation/Thermal Vapor Compression Hybrid System for Brine Treatment and Salt Recovery. *Chem. Eng. Process.* **2020**, *152*, 107934.

(8) Sharaf Eldean, M. A.; Fath, H. E. Exergy and Thermo-Economic Analysis of Solar Thermal Cycles Powered Multi-Stage Flash Desalination Process. *Desalin. Water Treat.* **2013**, *51*, 7361−7378.

(9) Kang, G.-d.; Cao, Y.-m. Development of Antifouling Reverse Osmosis Membranes for Water Treatment: A Review. *Water Res.* **2012**, *46*, 584−600.

(10) Lee, H.; Jin, Y.; Hong, S. Recent Transitions in Ultrapure Water (Upw) Technology: Rising Role of Reverse Osmosis (Ro). *Desalination* **2016**, *399*, 185−197.

(11) Werber, J. R.; Osuji, C. O.; Elimelech, M. Materials for Next-Generation Desalination and Water Purification Membranes. *Nat. Rev. Mater.* **2016**, *1*, 16018.

(12) Ghaffour, N.; Missimer, T. M.; Amy, G. L. Technical Review and Evaluation of the Economics of Water Desalination: Current and Future Challenges for Better Water Supply Sustainability. *Desalination* **2013**, *309*, 197−207.

(13) Guo, Y.; Lu, H.; Zhao, F.; Zhou, X.; Shi, W.; Yu, G. Biomass-Derived Hybrid Hydrogel Evaporators for Cost-Effective Solar Water Purification. *Adv. Mater.* **2020**, *32*, 1907061.

(14) Zhou, S.; Huang, S.; Ming, Y.; Long, Y.; Liang, H.; Ruan, S.; Zeng, Y.-J.; Cui, H. A Scalable, Eco-Friendly, and Ultrafast Solar Steam Generator Fabricated Using Evolutional 3d Printing. *J. Mater. Chem. A* **2021**, *9*, 9909−9917.

(15) Lu, H.; Shi, W.; Zhao, F.; Zhang, W.; Zhang, P.; Zhao, C.; Yu, G. High-Yield and Low-Cost Solar Water Purification via Hydrogel-Based Membrane Distillation. *Adv. Funct. Mater.* **2021**, *31*, 2101036.

(16) Zhang, L.; Bai, B.; Hu, N.; Wang, H. Low-Cost and Facile Fabrication of a Candle Soot/Adsorbent Cotton 3d-Interfacial Solar Steam Generation for Effective Water Evaporation. *Sol. Energy Mater. Sol. Cells* **2021**, *221*, 110876.

(17) Feng, J.; Bai, B.; Yang, L.; Hu, N.; Wang, H. Low-Cost and Facile Hydrophilic Amplification of Raw Corn Straws for the Applications of Highly Efficient Interfacial Solar Steam Generation. *Mater. Chem. Phys.* **2021**, *271*, 124904.

(18) Ibrahim, I.; Bhoopal, V.; Seo, D. H.; Afsari, M.; Shon, H. K.; Tijing, L. D. Biomass-Based Photothermal Materials for Interfacial

Solar Steam Generation: A Review. *Mater. Today Energy* **2021**, *21*, 100716.

(19) Fu, Q.; Li, X.; Ma, N.; Shi, D.; Chen, P.; Sun, J. Volcanic Relationship between Wettability of the Interface and Water Migration Rate in Solar Steam Generation Systems. *Nano Res.* **2021**, DOI: 10.1007/s12274-021-3631-5.

(20) Yao, H.; Zhang, P.; Yang, C.; Liao, Q.; Hao, X.; Huang, Y.; Zhang, M.; Wang, X.; Lin, T.; Cheng, H.; Yuan, J.; Qu, L. Janus-Interface Engineering Boosting Solar Steam Towards High-Efficiency Water Collection. *Energy Environ. Sci.* **2021**, *14*, 5330−5338.

(21) Gan, Q.; Zhang, T.; Chen, R.; Wang, X.; Ye, M. Simple, Low-Dose, Durable, and Carbon-Nanotube-Based Floating Solar Still for Efficient Desalination and Purification. *ACS Sustainable Chem. Eng.* **2019**, *7*, 3925−3932.

(22) Wang, M.; Wang, P.; Zhang, J.; Li, C.; Jin, Y. A Ternary Pt/Au/TiO2-Decorated Plasmonic Wood Carbon for High-Efficiency Interfacial Solar Steam Generation and Photodegradation of Tetracycline. *ChemSusChem* **2019**, *12*, 467−472.

(23) Tao, P.; Ni, G.; Song, C.; Shang, W.; Wu, J.; Zhu, J.; Chen, G.; Deng, T. Solar-Driven Interfacial Evaporation. *Nat. Energy* **2018**, *3*, 1031−1041.

(24) Dao, V.-D.; Choi, H.-S. Carbon-Based Sunlight Absorbers in Solar-Driven Steam Generation Devices. *Global Challenges* **2018**, *2*, 1700094.

(25) Ni, G.; Li, G.; Boriskina, S. V.; Li, H.; Yang, W.; Zhang, T.; Chen, G. Steam Generation under One Sun Enabled by a Floating Structure with Thermal Concentration. *Nat. Energy* **2016**, *1*, 16126.

(26) Jin, H.; Lin, G.; Bai, L.; Zeiny, A.; Wen, D. Steam Generation in a Nanoparticle-Based Solar Receiver. *Nano Energy* **2016**, *28*, 397−406.

(27) Tahir, Z.; Kim, S.; Ullah, F.; Lee, S.; Lee, J.-h.; Park, N.-W.; Seong, M.-J.; Lee, S.-K.; Ju, T.-S.; Park, S.; Bae, J.-S.; Jang, J. I.; Kim, Y. S. Highly Efficient Solar Steam Generation by Glassy Carbon Foam Coated with Two-Dimensional Metal Chalcogenides. *ACS Appl. Mater. Interfaces* **2019**, *12*, 2490−2496.

(28) Zhao, F.; Guo, Y.; Zhou, X.; Shi, W.; Yu, G. Materials for Solar-Powered Water Evaporation. *Nat. Rev. Mater.* **2020**, *5*, 388−401.

(29) Liu, G.; Xu, J.; Wang, K. Solar Water Evaporation by Black Photothermal Sheets. *Nano Energy* **2017**, *41*, 269−284.

(30) Irshad, M. S.; Wang, X.; Abbasi, M. S.; Arshad, N.; Chen, Z.; Guo, Z.; Yu, L.; Qian, J.; You, J.; Mei, T. Semiconductive, Flexible MnO2 Nws/Chitosan Hydrogels for Efficient Solar Steam Generation. *ACS Sustainable Chem. Eng.* **2021**, *9*, 3887−3900.

(31) Liu, X.; Mishra, D. D.; Li, Y.; Gao, L.; Peng, H.; Zhang, L.; Hu, C. Biomass-Derived Carbonaceous Materials with Multichannel Waterways for Solar-Driven Clean Water and Thermoelectric Power Generation. *ACS Sustainable Chem. Eng.* **2021**, *9*, 4571−4582.

(32) Wu, S.-L.; Chen, H.; Wang, H.-L.; Chen, X.; Yang, H.-C.; Darling, S. B. Solar-driven evaporators for water treatment: challenges and opportunities. *Environ. Sci.: Water Res. Technol.* **2021**, *7*, 24−39.

(33) Yang, H. C.; Chen, Z.; Xie, Y.; Wang, J.; Elam, J. W.; Li, W.; Darling, S. B. Solar Steam: Chinese Ink: A Powerful Photothermal Material for Solar Steam Generation (Adv. Mater. Interfaces 1/2019). *Adv. Mater. Interfaces* **2019**, *6*, 1970002.

(34) Zeng, Y.; Wang, K.; Yao, J.; Wang, H. Hollow Carbon Beads for Significant Water Evaporation Enhancement. *Chem. Eng. Sci.* **2014**, *116*, 704−709.

(35) Ren, P.; Yang, X. Synthesis and Photo-Thermal Conversion Properties of Hierarchical Titanium Nitride Nanotube Mesh for Solar Water Evaporation. *Sol. RRL* **2018**, *2*, 1700233.

(36) Li, H.; Jia, D.; Ding, M.; Zhou, L.; Wang, K.; Liu, J.; Liu, C.-Y.; Li, C. Robust 3d Graphene/Cellulose Nanocrystals Hybrid Lamella Network for Stable and Highly Efficient Solar Desalination. *Sol. RRL* **2021**, *5*, 2100317.

(37) Chen, Y.; Shi, Y.; Kou, H.; Liu, D.; Huang, Y.; Chen, Z.; Zhang, B. Self-Floating Carbonized Tissue Membrane Derived from Commercial Facial Tissue for Highly Efficient Solar Steam Generation. *ACS Sustainable Chem. Eng.* **2019**, *7*, 2911−2915.

(38) Chen, J.; Yang, B.; Li, H.; Ma, P.; Lang, J.; Yan, X. Candle Soot: Onion-Like Carbon, an Advanced Anode Material for a Potassium-Ion Hybrid Capacitor. *J. Mater. Chem. A* **2019**, *7*, 9247−9252.

(39) Raj, C. J.; Kim, B. C.; Cho, B.-B.; Cho, W.-J.; Kim, S.-J.; Park, S. Y.; Yu, K. H. Electrochemical Supercapacitor Behaviour of Functionalized Candle Flame Carbon Soot. *Bull. Mater. Sci.* **2016**, *39*, 241−248.

(40) Liang, C.-J.; Liao, J.-D.; Li, A.-J.; Chen, C.; Lin, H.-Y.; Wang, X.-J.; Xu, Y.-H. Relationship between Wettabilities and Chemical Compositions of Candle Soots. *Fuel* **2014**, *128*, 422−427.

(41) Azad, P.; Singh, V. P.; Vaish, R. Candle Soot-Driven Performance Enhancement in Pyroelectric Energy Conversion. *J. Electron. Mater.* **2018**, *47*, 4721−4730.

(42) Xiao, L.; Zeng, W.; Liao, G.; Yi, C.; Xu, Z. Thermally and Chemically Stable Candle Soot Superhydrophobic Surface with Excellent Self-Cleaning Properties in Air and Oil. *ACS Appl. Nano Mater.* **2018**, *1*, 1204−1211.

(43) Faizal, F.; Khairunnisa, M. P.; Yokote, S.; Lenggoro, I. W. Carbonaceous Nanoparticle Layers Prepared using Candle Soot by Direct- and Spray-based Depositions. *Aerosol Air Qual. Res.* **2018**, *18*, 856−865.

(44) Nevalainen, P.; Kinnunen, N.; Suvanto, M. Developmental Study of Soot-Oxidation Catalysts for Fireplaces: The Effect of Binder and Preparation Techniques on Catalyst Texture and Activity. *Catalysts* **2019**, *9*, 957.

(45) Yuan, Z.; Huang, J.; Peng, C.; Wang, M.; Wang, X.; Bin, J.; Xing, S.; Xiao, J.; Zeng, J.; Xiao, X.; Fu, X.; Gong, H.; Zhao, D.; Chen, H. Facile Preparation of Superhydrophobic Candle Soot Coating and Its Wettability under Condensation. *Appl. Phys. A* **2016**, *122*, 125.

(46) Ramires, M. L. V.; Nieto de Castro, C. A.; Nagasaka, Y.; Nagashima, A.; Assael, M. J.; Wakeham, W. A. Standard Reference Data for the Thermal Conductivity of Water. *J. Phys. Chem. Ref. Data* **1995**, *24*, 1377−1381.

(47) Zhang, Y.; Cao, S.; Qiu, Z.; Yin, K.; Lei, Y.; Sun, K.; Chang, X.; Li, X.; Fan, R. In situ chemo-polymerized polypyrrole-coated filter paper for high-efficient solar vapor generation. *Int. J. Energy Res.* **2020**, *44*, 1191−1204.

(48) Deng, Z.; Liu, P.-F.; Zhou, J.; Miao, L.; Peng, Y.; Su, H.; Wang, P.; Wang, X.; Cao, W.; Jiang, F.; Sun, L.; Tanemura, S. A Novel Ink-Stained Paper for Solar Heavy Metal Treatment and Desalination. *Sol. RRL* **2018**, *2*, 1800073.

(49) Liu, Z.; Song, H.; Ji, D.; Li, C.; Cheney, A.; Liu, Y.; Zhang, N.; Zeng, X.; Chen, B.; Gao, J.; Li, Y.; Liu, X.; Aga, D.; Jiang, S.; Yu, Z.; Gan, Q. Extremely Cost-Effective and Efficient Solar Vapor Generation under Nonconcentrated Illumination Using Thermally Isolated Black Paper. *Global Challenges* **2017**, *1*, 1600003.

(50) Ni, G.; Zandavi, S. H.; Javid, S. M.; Boriskina, S. V.; Cooper, T. A.; Chen, G. A salt-rejecting floating solar still for low-cost desalination. *Energy Environ. Sci.* **2018**, *11*, 1510−1519.